PTEP

Prog. Theor. Exp. Phys. **2014**, 113C01 (12 pages)
DOI: 10.1093/ptep/ptu152

Observation of coherent two-photon emission from the first vibrationally excited state of hydrogen molecules

Yuki Miyamoto[1], Hideaki Hara[1], Susumu Kuma[1,†], Takahiko Masuda[1], Itsuo Nakano[1], Chiaki Ohae[2,‡], Noboru Sasao[1,*], Minoru Tanaka[3], Satoshi Uetake[4,*], Akihiro Yoshimi[1], Koji Yoshimura[1], and Motohiko Yoshimura[4]

[1]*Research Core for Extreme Quantum World, Okayama University, Okayama 700-8530, Japan*
[2]*Graduate School of Natural Science and Technology, Okayama University, Okayama 700-8530, Japan*
[3]*Department of Physics, Osaka University, Toyonaka, Osaka 560-0043, Japan*
[4]*Research Center of Quantum Universe, Okayama University, Okayama 700-8530, Japan*
*E-mail: sasao@okayama-u.ac.jp, uetake@okayama-u.ac.jp

Received August 16, 2014; Revised October 15, 2014; Accepted October 15, 2014; Published November 24, 2014

In this paper, we describe an experiment which was conducted to explore the macro-coherent amplification mechanism using a two-photon emission process from the first vibrationally excited state of the para-hydrogen molecule. Large coherence in the initial state was prepared by the adiabatic Raman method, and the lowest Stokes sideband was used as a trigger field. We observed coherent two-photon emission consistent with the expectation of the Maxwell–Bloch equation derived for the process, whose rate is larger by many orders of magnitude than that of spontaneous emission.

Subject Index B54, C41, I81

1. Introduction

Coherence among an ensemble of atoms or molecules mediated by radiation fields has shown a variety of remarkable phenomena, and has offered a platform for devising new tools and/or methods. One classical example of such coherence is superradiance [1] (for reviews, see [2,3]). In this case, excited atoms or molecules organize themselves into a coherent state via a series of spontaneous emissions, eventually resulting in explosive radiation pulses. Another example is the adiabatic Raman process studied in [4–7]. In this case, the coherence is used to generate a series of equally spaced sidebands which in turn enables one to create ultra-short pulses.

Recently, some authors have proposed using a new type of coherent amplification mechanism in order to study experimentally much-suppressed processes involving neutrinos [8–11]. The ultimate goal of the proposal is to investigate unknown neutrino properties such as their absolute masses, mass type (Dirac or Majorana), and CP-violating phases [8,10,11]. This amplification by coherence, termed macro-coherent amplification, is applicable to a process which emits plural particles. If outgoing particles satisfy a certain phase-matching condition, equivalent to the momentum conservation

[†]Present address: Atomic, Molecular and Optical Physics Laboratory, RIKEN, Wako, Saitama 351-0198, Japan
[‡]Present address: Department of Engineering Science, University of Electro-Communications, Chofu, Tokyo 182-8585, Japan

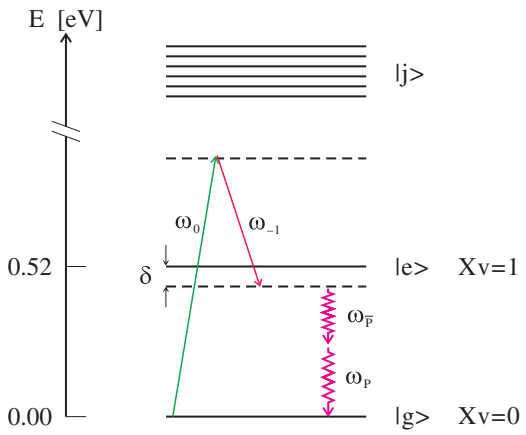

Fig. 1. Schematic diagram showing the relevant hydrogen molecule energy levels and the Raman excitation and two-photon emission processes.

law, then the process rate becomes proportional to N^2, where N is the number of coherent atoms or molecules involved in the process. When macro-coherent amplification is applied to the two-photon emission process, a pair of intense radiations may emerge in a similar fashion to the triggered superradiance.[1] Such a process, called paired superradiance (PSR), has been predicted, and its master equations have been derived [8,14]. In an ideal situation, most of the energy stored in an upper level may be released in an explosive way. The theory of PSR also predicts much milder events in which the degree of coherence, target number density, decoherence time, or a combination of these is less favorable than the explosive one [8].

In this paper, we describe an experiment which was conducted to explore the macro-coherent amplification mechanism using the two-photon emission process from the electronically ground vibrationally excited state ($|e\rangle$; $Xv = 1$) of hydrogen molecules. (For brevity, the word "hydrogen" will be used for hydrogen molecule below.) Figure 1 shows the hydrogen energy levels relevant to the present experiment. To prepare the initial states, we employed an adiabatic Raman method changing the hydrogen from its ground ($|g\rangle$; $Xv = 0$) state to the superposed state of $|g\rangle$ and $|e\rangle$ by a pair of driving lasers (ω_0 and ω_{-1} in Fig. 1). Since the electric dipole (E1) transition is strictly forbidden from electronically ground vibrationally excited states of homonuclear diatomic molecules, deexcitation from $Xv = 1$ is via two-photon emission whose spontaneous rate is very small. The main reason for using hydrogen molecules lies in these points; namely, the well-established method of coherence production exists for the E1 forbidden excited states. Two-photon emissions (ω_p and $\omega_{\bar{p}}$ in Fig. 1) together with other Raman sidebands were detected in the present experiment, and their yields were compared with the theoretical expectations.

In the present work, the two driving lasers were injected in the same direction, and one of the generated sidebands was used as a trigger field. This experimental configuration has been discussed in the literature [15] in the context of the parametric down conversion. Our experimental results may be understood from this viewpoint; however, we employ a different approach in the explanations

[1] One important difference between PSR and superradiance is that PSR occurs only from coherent initial states upon the application of the trigger field by, e.g., lasers, whereas superradiance may be observed from fully excited (thus incoherent) initial states. In this respect, PSR is similar to triggered superradiance. For experimental investigations of trigger effects on the superradiance, see, for example, [12,13].

below, namely the viewpoint of adiabatic Raman excitation supplemented by paired superradiance.[2] The basic equation (Maxwell–Bloch) presented below is derived from this viewpoint.[3]

The rest of the paper is organized as follows. In the next section, we briefly describe theoretical aspects of paired superradiance and the adiabatic Raman process, and present a simulation method based on an effective Hamiltonian combined for both. They are nonlinear processes and thus demand numerical simulations to obtain various observables which can be compared directly with actual experimental data. Following these, we describe our experimental setup in Sect. 3. The results and conclusions are given in Sects. 4 and 5, respectively.

2. Theory and simulation

We begin our discussion by constructing an effective Hamiltonian which describes both two-photon emission and Raman excitation processes. The basic QED interaction is the electric dipole interaction (E1) represented by $-\vec{d}\cdot\vec{E}$ with $\vec{d}$ being the dipole moment and $\vec{E}$ the electric fields. (We will omit the vector notation below since all the fields treated in this paper are linearly polarized in the same direction.) In the present system, the E1 dipole interaction connects $|g\rangle$ and $|e\rangle$ through an intermediate state $|j\rangle$, which is taken as an electronically excited state. Many intermediate levels may contribute, as shown in Fig. 1, but in the following we consider only one for simplicity. Extension to the case of multiple levels is trivial, and our actual simulation includes several tens of intermediate states [5]. The present system can be regarded as a two-level system once the intermediate state $|j\rangle$ is integrated out from the Schrödinger equation with the aid of the Markov approximation. The electromagnetic fields to be considered are the two driving lasers and the associated Raman sidebands with frequencies of

$$\omega_q = \omega_0 + q\Delta\omega, \quad \Delta\omega = \omega_0 - \omega_{-1}, \tag{1}$$

where the Raman order q is a positive (anti-Stokes) or negative (Stokes) integer satisfying $\omega_q > 0$. In the present experimental conditions, the smallest q (the lowest Stokes sideband) is $q = -4$. The frequency difference of the two driving lasers $\Delta\omega$ should be chosen to be nearly on resonance; the difference between the exact resonance frequency $\omega_{eg} \equiv \omega_e - \omega_g$ and $\Delta\omega$ is the detuning $\delta \equiv \omega_{eg} - \Delta\omega$. In addition to these sidebands, there should be the fields corresponding to the two-photon emissions. The frequencies of the pair are denoted by ω_p and $\omega_{\bar{p}}$ which should satisfy the energy conservation law of

$$\omega_p + \omega_{\bar{p}} = \Delta\omega. \tag{2}$$

Since the Raman excitation imprints a spatially dependent phase of $e^{i\Delta\omega\cdot x/c}$ in the medium, Eq. (2) satisfies the momentum conservation law if the two-photon fields propagate in the same direction as the excitation fields, and the dispersion in the medium is negligible for these wavelengths. The macro-coherent amplification mechanism requires the momentum conservation as well as the energy

[2] The PSR master equation accommodates a broad scope of two-photon-related phenomena. As already mentioned, it predicts explosive events. In addition, soliton formation (important to neutrino mass spectroscopy) occurs when lasers are irradiated in counter-propagating directions. For more detail, see [16]. These new phenomena are not explained in the idea of parametric down conversion.

[3] The Bloch equation, not explicitly written in Ref. [15], is necessary to take into account the detailed behavior of atoms. Comparison of experimental data with numerical simulations is done based on the Maxwell–Bloch equation in this paper.

Table 1. Wavelengths important in the present experiment.*

name	wavelength [nm]	symbols	remark
Energy gap ($\|e\rangle - \|g\rangle$)	2403.172	ω_{eg}	Ref. [17]
Driving laser (ω_0)	532.216	ω_0	measured
Driving laser (ω_{-1})	683.610	ω_{-1}	measured
Lowest Raman sideband	4662.48	$\omega_{-4} = \omega_{\bar{p}}$	calculated
Two-photon partner	4959.43	ω_p	calculated

*Note: All the values are at the pressure of 60 kPa except ω_{eg} which is the value of the zero pressure (collisionless) limit.

conservation of the elementary process. All the electromagnetic fields are taken to be traveling in one direction (taken to be x), and are expressed by

$$\tilde{E}_m(t,x) = \frac{1}{2}E_m(t,x)e^{-i\omega_m(t-x/c)} + c.c., \tag{3}$$

where m denotes either p, $\bar{p}$, or q, and E_m is the slowly varying envelope function. For future reference, we list the important frequencies in terms of wavelength in Table 1.

In order to proceed further, we resort to the standard technique of rotating wave approximation (RWA) and slowly varying envelope approximation (SVEA; see, for example, [18] and [19]). When these are applied to the Schrödinger equation, it turns out that the Raman process as well as the two-photon emission are described by the Hamiltonian $H = H_0 + H_1 + H_2$ of the form

$$H_0 = -\frac{1}{4}\sum_{m=p,\bar{p},q}\begin{pmatrix}\varepsilon_0\,\alpha_{gg}^{(m)}|E_m|^2 & 0\\ 0 & \varepsilon_0\,\alpha_{ee}^{(m)}|E_m|^2 - 4\hbar\delta\end{pmatrix}, \tag{4}$$

$$H_1 = -\frac{1}{4}\sum_{q=-4}^{\infty}\begin{pmatrix}0 & \varepsilon_0\,\alpha_{ge}^{(q)}E_q E_{q+1}^*\\ \varepsilon_0\,\alpha_{eg}^{(q)}E_q^* E_{q+1} & 0\end{pmatrix}, \tag{5}$$

$$H_2 = -\frac{1}{4}\begin{pmatrix}0 & \varepsilon_0\,\alpha_{ge}^{(p\bar{p})}E_p^* E_{\bar{p}}^*\\ \varepsilon_0\,\alpha_{eg}^{(p\bar{p})}E_p E_{\bar{p}} & 0\end{pmatrix}, \tag{6}$$

where H_0 gives the Stark energy shift with the detuning δ, H_1 the adiabatic Raman process derived in [4,7], and H_2 the two-photon emission which can be reduced from the paired superradiance master equation when electromagnetic propagations are assumed unidirectional [8,14]. In Eq. (4), $\alpha_{gg}^{(m)}$ or $\alpha_{ee}^{(m)}$ is the polarizability of the state $|g\rangle$ or $|e\rangle$, and is given by[4]

$$\alpha_{aa}^{(m)} = \frac{|d_{aj}|^2}{\varepsilon_0\hbar}\left(\frac{1}{\omega_{ja}+\omega_m} + \frac{1}{\omega_{ja}-\omega_m}\right), \quad (a = g, e;\ m = p, \bar{p}, q) \tag{7}$$

[4] The polarizability α_{gg} is related to the index of refraction by $n_r \simeq 1 + n\alpha_{gg}/2$ in the long wavelength limit, where n is the number density of the molecules.

where d_{aj} and $\hbar\omega_{ja} \equiv \hbar(\omega_j - \omega_a)$ are, respectively, a transition dipole moment and energy difference between levels $a - j$. Similarly, the off-diagonal parts of the polarizability in Eqs. (5) and (6) are given by

$$\alpha_{ge}^{(q)} = \alpha_{eg}^{(q)} = \frac{d_{gj}d_{je}}{\varepsilon_0\hbar}\left(\frac{1}{\omega_{jg}+\omega_q} + \frac{1}{\omega_{je}-\omega_q}\right), \tag{8}$$

$$\alpha_{ge}^{(p\bar{p})} = \alpha_{eg}^{(p\bar{p})} = \frac{d_{gj}d_{je}}{\varepsilon_0\hbar}\left(\frac{1}{\omega_{jg}-\omega_p} + \frac{1}{\omega_{jg}-\omega_{\bar{p}}}\right) = \frac{d_{gj}d_{je}}{\varepsilon_0\hbar}\left(\frac{1}{\omega_{je}+\omega_p} + \frac{1}{\omega_{je}+\omega_{\bar{p}}}\right). \tag{9}$$

In order to include relaxation effects, it is necessary to introduce the density matrix for a mixture of pure states:

$$\rho = \begin{pmatrix} \rho_{gg} & \rho_{ge} \\ \rho_{eg} & \rho_{ee} \end{pmatrix}. \tag{10}$$

The equation of motion for the density matrix is governed by $i\hbar(d\rho/dt) = [H, \rho] +$ (relaxation terms), and its explicit forms will be shown below. So far we have considered a single molecule, which is now extended to an ensemble of molecules within a finite volume. To this end, the density matrix is considered to be a function of the position x by taking a continuous limit of atom distribution in the target. We also need to consider a propagation effect of the electromagnetic fields: this effect is included by the one-dimensional Maxwell equation

$$\frac{\partial^2 E}{\partial t^2} - c^2\frac{\partial^2 E}{\partial x^2} = -\frac{n}{\varepsilon_0}\frac{\partial^2 P}{\partial t^2}, \tag{11}$$

where P denotes the macroscopic polarization, and n the number density of the hydrogen molecules. The polarization P can be calculated with $P = \mathrm{Tr}(\rho d)$. Putting P into Eq. (11) with the help of RWA and SVEA, we arrive at a set of equations, referred to as the Maxwell–Bloch equations, expressed by

$$\frac{\partial\rho_{gg}}{\partial\tau} = i(\Omega_{ge}\rho_{eg} - \Omega_{eg}\rho_{ge}) + \gamma_1\rho_{ee}, \tag{12}$$

$$\frac{\partial\rho_{ee}}{\partial\tau} = i\big(\Omega_{eg}\rho_{ge} - \Omega_{ge}\rho_{eg}\big) - \gamma_1\rho_{ee}, \tag{13}$$

$$\frac{\partial\rho_{ge}}{\partial\tau} = i\big(\Omega_{gg} - \Omega_{ee} + \delta\big)\rho_{ge} + i\Omega_{ge}\big(\rho_{ee} - \rho_{gg}\big) - \gamma_2\rho_{ge}, \tag{14}$$

$$\frac{\partial E_q}{\partial\xi} = \frac{i\omega_q n}{2c}\left\{\left(\rho_{gg}\alpha_{gg}^{(q)} + \rho_{ee}\alpha_{ee}^{(q)}\right)E_q + \rho_{eg}\alpha_{eg}^{(q-1)}E_{q-1} + \rho_{ge}\alpha_{ge}^{(q)}E_{q+1}\right\}, \tag{15}$$

$$\frac{\partial E_p}{\partial\xi} = \frac{i\omega_p n}{2c}\left\{\left(\rho_{gg}\alpha_{gg}^{(p)} + \rho_{ee}\alpha_{ee}^{(p)}\right)E_p + \rho_{eg}\alpha_{ge}^{(p\bar{p})}E_{\bar{p}}^*\right\}. \tag{16}$$

Here we have introduced the co-moving coordinates defined by $(\tau, \xi) = (t - x/c, x)$, and the Rabi frequencies by

$$\Omega_{aa} = \frac{1}{2\hbar}\sum_{m=p,\bar{p},q}\frac{1}{2}\varepsilon_0\,\alpha_{aa}^{(m)}|E_m|^2 \quad (a = g, e),$$

$$\Omega_{ge} = \Omega_{eg}^* = \frac{1}{2\hbar}\left\{\sum_q\frac{1}{2}\varepsilon_0\,\alpha_{ge}^{(q)}E_q E_{q+1}^* + \frac{1}{2}\varepsilon_0\,\alpha_{ge}^{(p\bar{p})}E_p^*E_{\bar{p}}^*\right\}. \tag{17}$$

Relaxation terms in the Bloch equations (12)–(14), given by the terms proportional to γ_1 (longitudinal) and γ_2 (transverse), are the most general form in the two-level system.

Numerical simulations are performed based upon the Maxwell–Bloch equations (12)–(16) shown above. As indicated in Table 1, the lowest ($q = -4$) Stokes sideband is used for the trigger field for the two-photon emission in this experiment: we thus take $\bar{p}$ as one of the two-photon pair and identify it with $q = -4$. Actually, in the Maxwell equation (15) for $q = -4$, the term $\rho_{eg}\alpha_{eg}^{(q-1)}E_{q-1}$ was replaced by $\rho_{eg}\alpha_{ge}^{(p\bar{p})}E_p^*$. As to the relaxation terms, the dominant contribution comes from γ_2, which is taken from experimental measurements [20]. In total, 51 intermediate states $|j\rangle$ are taken into account in the evaluation of the polarizabilities, and they are then rescaled so that they agree with the measured index of refraction [21]. The $1 + 1$-dimensional Maxwell–Bloch equation has an apparent shortcoming: it cannot treat any transverse effects, in particular the transverse intensity variation of the input lasers or the output radiations. In Sect. 4, we will present a practical method to circumvent this insufficiency together with the simulation results.

3. Experimental setup

A schematic diagram of the experimental setup is shown in Fig. 2. It consists of three major parts: the laser excitation system, the para-hydrogen (p-H_2) gas target, and the detector system. In this experiment, generation of the large target coherence is the key to success, and every care was taken to enhance it both in the laser and the target systems. In the following, we describe each in turn.

3.1. Laser system

We used the second harmonic of a Q-switched injection-seeded Nd:YAG laser ($\lambda = 532.216$ nm, Litron LPY642) as a master light source; all the required lasers are produced from this single laser to reduce temporal jitter between the two pulses. It is operated at a repetition rate of 10 Hz with a pulse duration of 8 ns and an energy up to 130 mJ. It has a single transverse mode ($M^2 < 1.1$) and a narrow linewidth (<100 MHz). Its beam is divided into three as shown in Fig. 2: one is delivered to the target as the ω_0 laser, and the other two are used as pumping light sources for the ω_{-1} laser.

For the ω_{-1} light ($\lambda = 683.610$ nm) generation, we built a laser system of an injection-seeded optical parametric generator (OPG) combined with an optical parametric amplifier (OPA). In the OPG stage, a nonlinear optical crystal of MgO-doped periodically poled stoichiometric lithium tantalate (PPSLT, Oxide Corp. Q1532-O001) is used; its dimension is 24 mm long × 1 mm thick ×8 mm wide, with a grating period of 10.3 μm. As an injection seeding laser for OPG, an extended cavity diode laser (ECDL) in the Littrow configuration is made using a commercially available laser diode chip (TOPTICA LD-0685-0050-3, no anti-reflection coating). The measured output power of the ECDL is more than 10 mW with a typical mode-hop-free scanning range of 3 GHz. The pumping (pulsed) and injection-seeding (continuous wave) laser lights are combined with a dichroic mirror, and then injected into the PPSLT crystal. A typical output pulse energy at the OPG stage is 0.4 mJ, and a linewidth is 97 MHz, nearly the Fourier-transform-limited linewidth. For the OPA stage, we used bulk lithium triborate (LBO) crystals in a noncritical phase-matching condition. The output pulse from the OPG is amplified to more than 6 mJ at the OPA stage.

The actual pulse energy and the beam waist size of the ω_0 (ω_{-1}) driving laser is 4.3 mJ (4.3 mJ) and 0.12 mm (0.15 mm), respectively. Both lasers are linearly polarized in the same direction. For the detuning (δ) scan, we changed the frequency of the ECDL seeding laser.

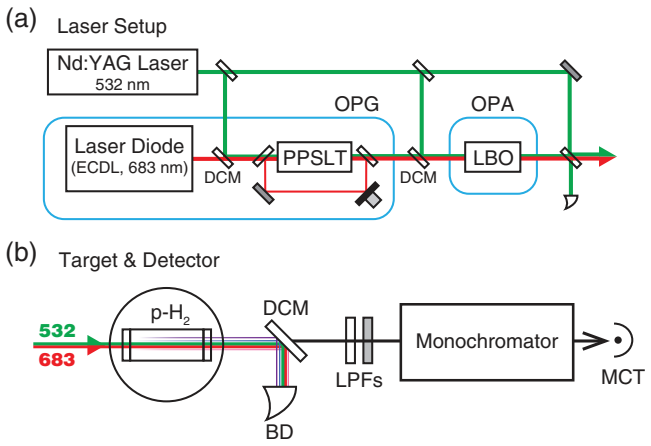

Fig. 2. Schematics of the experimental setup. (a) The laser system. The main Nd:YAG laser beam is divided into three beams. Two of them are used as pumping light sources to generate the ω_{-1} laser (683 nm) and the rest is used as the ω_0 laser (532 nm). For the ω_{-1} light generation, we employed an injection-seeded OPG with a PPSLT crystal and OPA with LBO crystals. A typical output power at the OPA stage is $\geq$6 mJ at 683 nm. (b) Schematic diagram of the target and the detector. DCM: dichroic mirror; BD: Beam dumper; LPFs: long-pass filters; MCT: Hg–Cd–Te mid-infrared detector.

3.2. Target

We used para-hydrogen (p-H_2 with purity of $<$500 ppm ortho-hydrogen contamination) gas at a temperature of 78 K as a target. The main reasons for using p-H_2 are that it is suited to observe two-photon emission from the E1 forbidden vibrationally excited state, and that the production technique of large coherence is well established. In addition to these, para-hydrogen has the merit of longer decoherence time over normal hydrogen (1 : 3 mixture of para- and ortho-hydrogen), and the low temperature (78 K) is better because the decoherence time (γ_2^{-1}) is nearly the longest thanks to Dicke narrowing [22,23].

The actual target, cylindrical, 20 mm in diameter and 150 mm in length, was installed in a cryostat. The pressure could be varied, but in the present experiment it was fixed at 60 kPa (the estimated number density assuming ideal gas is $n = 5.6 \times 10^{19}\,\mathrm{cm}^{-3}$). Both pressure and temperature were monitored constantly during the experiment. The estimated decoherence rate at this condition is about 130 MHz [8].

3.3. Detectors

As shown in Fig. 2(b), the lights exiting from the target cryostat window went through a dichroic mirror to reflect strong driving laser lights and a Ge filter to further reduce visible-region lights. They entered a monochromator (Princeton Instruments Acton SpectraPro SP2300) to analyze the wavelength of mid-infrared (MIR) lights. The wavelength resolution of the monochromator, having a grating of 150 groove mm^{-1} and 4 μm blaze wavelength, was set to about 1 nm to observe MIR spectra and to about 50 nm in other experiments. An actual MIR detector was MCT (HgCdTe, Daylight Solutions HPC-2TE-100). When the Raman sideband energy was measured, the system above was replaced with a prism and a pyroelectric energy detector (Gentec Electro-Optics QE12LP-H-MB). The MCT signals were monitored by an oscilloscope and were sent to a computer for later offline analysis. On average, 100–200 shots were accumulated at a single parameter setting.

4. Experimental results

4.1. Raman sidebands

We first show the results of Raman sideband measurements. Figure 3 shows a photograph of Raman sidebands taken by a CCD camera. As can be seen, we observed the anti-Stokes sidebands up to eighth order and the Stokes sidebands to second order. In the photograph, the short wavelength was limited by the absorption due to the air, and the long wavelength by the sensitivity of the CCD camera. They were all found to be collinear with the excitation lasers. Pulse energies of sidebands from $q = -3$ to $q = +4$ were measured by the pyroelectric energy detector. Figure 4 shows a comparison of the pulse energy measurements ($\delta = 0$) with the simulation results. The latter is obtained as follows. As explained in Sect. 2, the $1 + 1$-dimensional Maxwell–Bloch equation cannot handle transverse intensity variations. This fact demands that, in the simulation, it is necessary to use an averaged power to account for the transverse intensity variation of the excitation lasers. It also means that any radiation power obtained by the simulation must be multiplied by an angular variation factor (usually unknown) to compare with actual output energy measurements. For the input laser power, we left it free in the simulation, and determined it by seeking the best fit to the actual data.[5] For the output power, we obtain the required angular factor using one of the sideband data. In other words, all the simulation results (including the 4.96 μm emission) are multiplied by a common factor so that the chosen sideband pulse energy agrees with the corresponding experimental result. We actually chose $q = 1$ for this purpose (the normalization point). This choice is based on the considerations that the higher-order sidebands (especially $q > 2$) are prone to be affected by dispersion effects[6] and that the strong driving lasers are in general less sensitive to the development of coherence-producing processes. Note also that the best input power in the simulation is found to be about 0.062 (0.078) of the peak power for the ω_0 (ω_{-1}) laser.[5] As seen in Fig. 4, the overall agreement between the simulation and experimental results is satisfactory, although the simulation predicts lower power for large q.[6] From this simulation result, we can estimate an average degree of coherence along the target: it is $\rho_{ge} \simeq 0.032$ at $\tau = 0$, the peak timing of the driving lasers.

[5] We note that the Raman sidebands are generated only from the overlapped volume of the two driving lasers; however, they do not overlap completely in general. Taking this possibility into account, we treated their effective intensities independently, and minimized the χ^2 defined by

$$\chi^2 = \sum_{q \neq 0,-1} \left(\frac{P_q^{\mathrm{exp}}(\delta = 0) - P_q^{\mathrm{sim}}(\delta = 0)}{P_q^{\mathrm{exp}}(\delta = 0)} \right)^2 , \tag{18}$$

where $P_q^{\mathrm{exp}}(\delta = 0)$ ($P_q^{\mathrm{sim}}(\delta = 0)$) denotes the qth sideband power normalized at $q = 1$ obtained by the experiment (simulation) at the detuning $\delta = 0$. The summation runs from $q = -3$ to $q = 3$, excluding $q = 0$ and $q = -1$. These powers, corresponding to the two driving lasers (ω_0 and ω_{-1}), should be excluded from the χ^2 sum because they may contain ineffective ones (non-overlapping part).

[6] There is a discrepancy between the real and simulation data for $q > 2$. One possible source is the dispersion effect (frequency variation of the refractive index) which is much stronger in the short wavelength region ($q > 2$). The dispersion effect causes phase mismatch between fields and/or coherence (i.e. the momentum conservation law does not hold). In the real experiment, this phase mismatch can be avoided, at least partially, by emitting lights at slightly different directions. However, the $1 + 1$-dimensional simulation fails to include such an effect, resulting in less power compared to the real data.

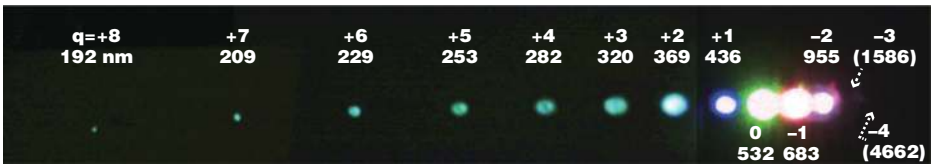

Fig. 3. Photograph of the Raman sidebands (projected onto a fluorescent sheet and taken by a CCD camera). The wavelengths calculated with Eq. (1) are also shown. The third and fourth Stokes sidebands shown in parentheses are observed only by the pyroelectric energy and/or MCT detector. The photograph contrast and light level from $q = 2$ to $q = 8$ are enhanced for a clear view. Apparent variation in the spot sizes is due to over-exposure while distortion from the straight line (around $q = 6$–8) is caused by bending of the fluorescent sheet.

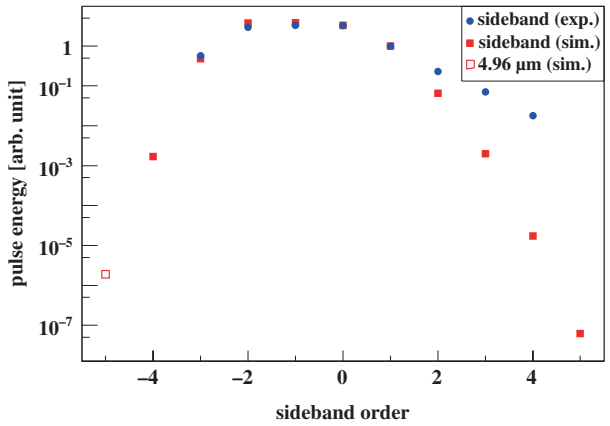

Fig. 4. Comparison of the Raman sideband pulse energy measurements (from $q = -3$ to $q = +4$ at $\delta = 0$) with the simulation results. The vertical axis represents energies (the simulation results are normalized at $q = 1$) while the horizontal axis is the Raman order q. The 4.96 μm signal is plotted at $q = -5$ for convenience. The circles in blue (squares in red) indicate the experimental (simulation) results.

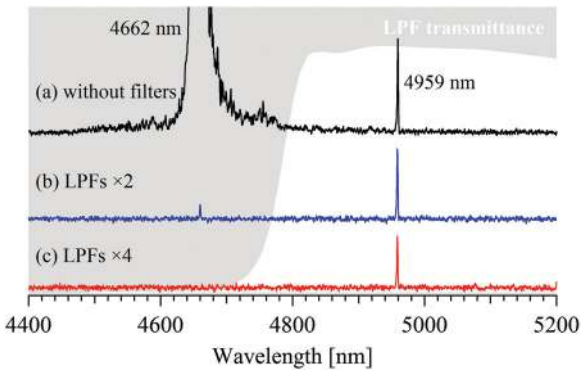

Fig. 5. Observed spectra at $\delta = 0$ MHz and 60 kPa; (a) without the long-pass filter (LPF), (b) with two LPFs, and (c) with four LPFs. The white portion excluded by the gray hatching shows the LPF transmittance; it is ∼0.85 at 4.96 μm.

4.2. Two-photon emission process

Figure 5 shows the result of spectrum measurements at a detuning of $\delta = 0$. The black line is the spectrum without the long-pass filter (LPF, Spectrogon LP-4700nm) while the blue (red) line is that with two (four) LPFs inserted in front of the monochromator. The transmittance of the LPF is indicated by

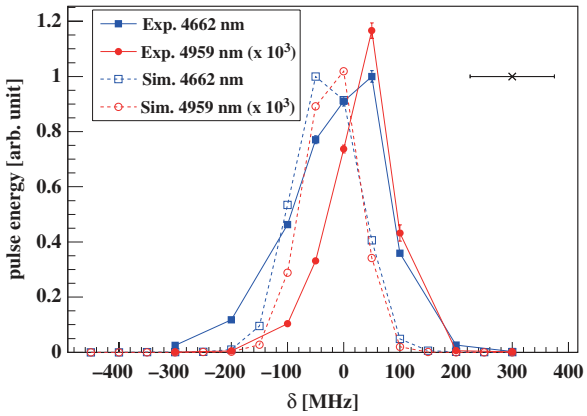

Fig. 6. The 4.66 and 4.96 μm output pulse energies as a function of the detuning frequency δ. The solid (open) symbols connected by solid (dashed) lines indicate the experimental (simulation) data. The red circles are for 4.96 μm (scaled up by 10^3) and the blue squares for 4.66 μm. The horizontal bar in the plot indicates ±75 MHz uncertainty in the frequency measurements.

the white portion excluded by the gray hatch. Two peaks were unambiguously observed corresponding to the fourth Stokes sideband (4.66 μm) and its two-photon partner (4.96 μm). The 4.66 μm signal saturated the detector without LPF, but was mostly filtered out with LPFs. On the other hand, the 4.96 μm signal remained unaffected with and without LPFs (the peak heights reduced by LPF transmittance of ∼0.85 per filter), which eliminates the possibility of spurious higher-order lights in the monochromator grating system. It was found that these signals had a sharp forward distribution (half angular divergence of ∼20 mrad for 4.66 μm and ∼10 mrad for 4.96 μm) and a time profile similar to the input driving lasers (with slightly narrower FWHM pulse durations of ∼5 ns). The latter can be interpreted as a measure of the duration time of the produced coherence. A typical 4.96 μm pulse energy observed by the MCT detector was 1.8 pJ/pulse (without acceptance correction of the monochromator), and the ratio of the two signals, defined by the 4.96 μm energies divided by those at 4.66 μm, was $\sim 0.8 \times 10^{-3}$ at this detuning.

4.3. Detuning curve

Figure 6 shows the pulse energies of the 4.66 and 4.96 μm pair as a function of the detuning δ (detuning curves). In the figure, the experimental data (indicated by solid squares and circles) are obtained by integrating each MCT output pulse while the simulation data (indicated by open squares and circles) are normalized in such a way that the maximum values of the 4.66 μm real and simulation data agree with each other. Thus, meaningful comparisons between the real data and simulations are the shape of the 4.66 and 4.96 μm detuning curves and their relative magnitude. As to the shape, the agreement between the real data and simulations is good. However, the peak positions of the real data (for both 4.66 and 4.96 μm) are slightly (∼100 MHz) higher than those of the simulation data. We note that absolute accuracy of the frequency determination is estimated to be ±75 MHz;[7] thus the difference in the peak positions may stem from the uncertainty in the frequency measurements. As to the relative magnitude, the ratios of the 4.96 μm to 4.66 μm powers are of the order of 10^{-3} both

[7] The main source of uncertainties comes from the absolute accuracy in the wavelength meter (HighFinesse WS-7).

for the real and simulation data, showing good agreement with each other. In any case, the overall agreement between the simulation and experimental results is regarded as reasonable.

For illustrative purpose, we compare below the 4.96 μm absolute pulse energy with the spontaneous two-photon decay. To this end, the measured outputs are corrected for various transmittance or reflection efficiencies of the optical elements, except for the monochromator efficiency which is assumed to be unity.[8] The resulting value, converted to the number of photons per pulse, is 4.4×10^7. As to the spontaneous decay process, we have estimated it as follows. Its rate (A) is expressed by

$$\frac{dA}{dz} = \frac{\omega_{eg}^7}{(2\pi)^3 c^6} \left|\alpha_{ge}^{(p\bar{p})}\right|^2 z^3(1-z)^3 \sim 3.2 \times 10^{-11}\ \text{1/s} \quad \left(z = \frac{1}{2}\right), \tag{19}$$

where $z = \omega/\omega_{eg}$ is the fractional energy of one of the two photons. Considering the energy bandwidth $\Delta z \sim 4.9 \times 10^{-3}$ (taken to be the monochromator full width), the measurement time $\Delta t \sim 80$ [ns], the detector solid angle fraction $\Delta\Omega/(4\pi) \sim 1.2 \times 10^{-4}$ (for which the monochromator efficiency is assumed to be unity), and the maximum number of excited states in the target ($\sim 1.5 \times 10^{16}$), we obtained the number of expected photons to be 1.6×10^{-8} per pulse. This value may be compared to 4.4×10^7, which is a lower bound for the photons actually observed: the huge enhancement factor ($>10^{15}$) can only be understood in the presence of macro-coherence.

5. Conclusions and summary

In this paper, we have described an experiment which was conducted to explore the macro-coherent amplification mechanism using the two-photon emission process from the para-hydrogen electronically ground vibrationally excited state ($Xv = 1$). The adiabatic Raman method was employed to prepare large coherence in the initial state. The Raman sidebands from the lowest Stokes ($q = -4$) up to the eighth anti-Stokes ($q = 8$) were observed and their intensities were compared to a simulation based upon the Maxwell–Bloch equation in order to estimate the degree of coherence. With the lowest Stokes sideband ($\lambda = 4.66\,\mu$m) used as a trigger, the two-photon emission partner ($\lambda = 4.96\,\mu$m) was seen unambiguously. The observed two-photon rate is found to be much larger than that of the two-photon spontaneous decay, and to be consistent with the expectation of the Maxwell–Bloch equation derived for the process. Although the macro-coherence amplification mechanism deserves further examination, the present experimental results support its basic principle in the non-explosive regime.

Acknowledgements

We thank Professors K. Kawaguchi and T. Momose for valuable discussions. We are deeply indebted to Prof. M. Katsuragawa for his advice on the adiabatic Raman process. This research was partially supported by Grant-in-Aid for Scientific Research on Innovative Areas "Extreme quantum world opened up by atoms" (21104002), Grant-in-Aid for Scientific Research A (21244032), Grant-in-Aid for Scientific Research C (25400257), Grant-in-Aid for Challenging Exploratory Research (24654132), and Grant-in-Aid for Young Scientists B (25820144) from the Ministry of Education, Culture, Sports, Science, and Technology.

References

[1] R. H. Dicke, Phys. Rev. **93**, 99 (1954).

[8] The monochromator efficiency depends on the spot size and angular divergence of input lights and/or grating efficiency, which in turn depends on the wavelength. It is difficult to measure this efficiency accurately without a good MIR calibration light source. The number of photons quoted in the paper thus represents the lower bound.

[2] M. Benedict, A. M. Ermolaev, V. A. Malyshev, I. V. Sokolov, and E. D. Trifonov, *Super-radiance; Multiatomic Coherent Emission* (Taylor & Francis, New York, 1996).
[3] M. Gross and S. Haroche, Phys. Rep. **93**, 301 (1982).
[4] S. E. Harris and A. V. Sokolov, Phys. Rev. **A55**, R4019 (1997).
[5] F. Le Kien, J. Q. Liang, M. Katsuragawa, K. Ohtsuki, K. Hakuta, and A. V. Sokolov, Phys. Rev. **A60**, 1562 (1999).
[6] A. V. Sokolov, D. R. Walker, D. D. Yavuz, G. Y. Yin, and S. E. Harris, Phys. Rev. Lett. **85**, 562 (2000).
[7] J. Q. Liang, M. Katsuragawa, F. Le Kien, and K. Hakuta, Phys. Rev. Lett. **85** 2474 (2000).
[8] A. Fukumi, S. Kuma,Y. Miyamoto,K. Nakajima,I. Nakano, H. Nanjo, C. Ohae, N. Sasao, M. Tanaka, T. Taniguchi, S. Uetake, T. Wakabayashi, T. Yamaguchi, A. Yoshimi, and M. Yoshimura, Prog. Theor. Exp. Phys. 04D002 (2012).
[9] M. Yoshimura, C. Ohae, A. Fukumi, K. Nakajima, I. Nakano, H. Nanjo, and N. Sasao, [arXiv:0805.1970 [hep-ph]] [Search INSPIRE].
[10] D. N. Dinh, S. T. Petcov, N. Sasao, M. Tanaka, and M. Yoshimura, Phys. Lett. **B719**, 154 (2013) [arXiv:1209.4808] [Search INSPIRE].
[11] M. Yoshimura and N. Sasao, Phys. Rev. **D89**, 053013 (2014) [arXiv:1310.6472] [Search INSPIRE].
[12] N. W. Carlson, D. J. Jackson, A. L. Schawlow, M. Gross, and S. Haroche, Opt. Commun. **32**, 350 (1980).
[13] C. Ohae, A. Fukumi, S. Kuma, Y. Miyamoto, K. Nakajima, I. Nakano, H. Nanjo, N. Sasao, S. Uetake, T. Wakabayashi, A. Yoshimi, K. Yoshimura, and M. Yoshimura, J. Phys. Soc. Jpn. **83**, 044301 (2014).
[14] M. Yoshimura, N. Sasao, and M. Tanaka, Phys. Rev. **A86** 013812 (2012).
[15] S. E. Harris and M. Jain, Optics Lett. **22**, 636 (1997).
[16] M. Yoshimura and N. Sasao, Prog. Theor. Exp. Phys. 073B02 (2014).
[17] G. D. Dickenson, M. L. Niu, E. J. Salumbides, J. Komasa, K. S. E. Eikema, K. Pachucki, and W. Ubachs, Phys. Rev. Lett. **110**, 193601 (2013).
[18] Y. B. Band, *Light and Matter* (John Wiley & Sons, West Sussex, 2006).
[19] C. J. Foot, *Atomic Physics* (Oxford University Press, Oxford, 2005).
[20] W. B. Bischel and M. J. Dyer, Phys. Rev. **A33**, 3113 (1986).
[21] S. W. Huang, W. Chen, and A. H. Kung, Phys. Rev. **A74**, 063825 (2006).
[22] R. H. Dicke, Phys. Rev. **89**, 472 (1953).
[23] W. B. Bischel and M. J. Dyer, Phys Rev. **A33**, 3113 (1986).